Zonal flow reversals in two-dimensional Rayleigh-Bénard convection

P. Winchester,* V. Dallas,† and P. D. Howell‡
Mathematical Institute, University of Oxford, Oxford OX2 6GG, United Kingdom

(Received 3 November 2020; accepted 2 March 2021; published 22 March 2021)

Using long-time direct numerical simulations, we analyze the reversals of the large scale zonal flow in two-dimensional Rayleigh-Bénard convection with a rectangular geometry of aspect ratio Γ. We impose periodic and free-slip boundary conditions in the streamwise and spanwise directions, respectively. As Rayleigh number Ra increases, large scale flow dominates the dynamics of a moderate Prandtl number fluid. At high Ra, transitions are seen in the probability density function (PDF) of the largest scale mode. For $\Gamma = 2$, the PDF first transitions from a Gaussian to a trimodal behavior, signifying the emergence of large scale flow reversals, where the flow fluctuates between three distinct states: two states in which a zonal flow travels in opposite directions and one state with no zonal mean flow. Further increase in Ra leads to a transition from a trimodal to a unimodal PDF which demonstrates the disappearance of the zonal flow reversals. On the other hand, for $\Gamma = 1$, the zonal flow reversals are characterized by a bimodal PDF of the largest scale mode, where the flow fluctuates only between two distinct states with zonal flow traveling in opposite directions.

DOI: 10.1103/PhysRevFluids.6.033502

I. INTRODUCTION

Large scale zonal flow in buoyancy-driven convection is found in the atmosphere of Jupiter [1–3], in the Earth's oceans [4–6], in nuclear fusion devices [7,8], in laboratory experiments [9–11], and recently in numerical simulations of Rayleigh-Bénard convection [12–15]. This large scale flow can undergo abrupt transitions, seemingly randomly, after very long periods of apparent stability [16,17].

Such transitions have been observed in a wide range of turbulent flows, including flow past bluff bodies [18,19], von Kármán flow [20–22], reversals in a dynamo experiment [23], Rayleigh-Bénard convection [24,25], Taylor-Couette flow [26], experiments on two-dimensional (2D) turbulence [27], and Kolmogorov flow [28]. In the turbulent regime, the broken symmetries of the flow can be restored statistically [29]. However, these flows undergo transitions, which lead to different flow states as a control parameter increases, and correspond to spontaneous symmetry breaking in a system far from equilibrium.

In Rayleigh-Bénard convection, such transitions have also been observed in the form of reversals of the large scale flow in various setups [30–32]. In particular, reversals of the large scale circulation (LSC) in an enclosed rectangular geometry have been observed in several experiments and numerical simulations [33–40].

In this article, we report on the reversals of the large scale zonal flow that emerge in 2D Rayleigh-Bénard convection. These transitions occur between long-lived metastable states on a

*winchester@maths.ox.ac.uk
†vassilios.dallas@maths.ox.ac.uk
‡howell@maths.ox.ac.uk

fluctuating background, and thus resemble phase transitions in condensed matter physics [41]. Thus, the present work could be of interest to a wider range of fields beyond fluid dynamics. Moreover, the zonal flow reversals are found in the classical Rayleigh-Bénard convection setup of a rectangular geometry, with periodic and free-slip boundary conditions in the streamwise and spanwise directions, respectively. On this idealized setup, the flow field can be decomposed into convenient basis functions, which allow further theoretical development.

II. PROBLEM DESCRIPTION

We adopt the Boussinesq approximation, assuming constant kinematic viscosity ν, and thermal diffusivity κ. The resulting equations governing 2D Rayleigh-Bénard convection, written in terms of the stream function $\psi(x, y, t)$ and the perturbation $\theta(x, y, t)$ from the steady state temperature, are

$$\psi_t + \nabla^{-2}\{\psi, \nabla^2\psi\} = g\alpha\nabla^{-2}\theta_x + \nu\nabla^2\psi, \tag{1}$$

$$\theta_t + \{\psi, \theta\} = \frac{\Delta T}{\pi d}\psi_x + \kappa\nabla^2\theta, \tag{2}$$

where $\{f, g\} = f_x g_y - g_x f_y$ is the standard Poisson bracket. Our spatial domain is bounded vertically by $y \in [0, \pi d]$ and horizontally by $x \in [0, 2\pi L]$. The imposed boundary conditions are periodic in x and free slip in the y direction, specifically $\psi(x, y, t) = \psi(x + 2\pi L, y, t)$, $\theta(x, y, t) = \theta(x + 2\pi L, y, t)$, and $\psi = \psi_{yy} = \theta = 0$ at $y = 0, \pi d$. The three nondimensional parameters are the aspect ratio $\Gamma = 2L/d$, the Prandtl number $\mathrm{Pr} = \nu/\kappa$, and the Rayleigh number $\mathrm{Ra} = \alpha g \Delta T (\pi d)^3/(\nu\kappa)$, where α is the thermal expansion coefficient, ΔT is the temperature difference between the top and bottom plates, and g is the gravitational acceleration. In this study, we fix $\mathrm{Pr} = 30$ and consider $\Gamma = 1$ and 2 for Ra ranging from 10^4 to 10^7.

We perform direct numerical simulations (DNSs) by integrating Eqs. (1) and (2) using the pseudospectral method [42]. Based on the numerical code from [28,43] we decompose the stream function into basis functions with Fourier modes in the x direction and sine modes in the y direction, viz.,

$$\psi(x, y, t) = \sum_{k_x=-N_x/2}^{N_x/2} \sum_{k_y=1}^{N_y} \widehat{\psi}_{k_x,k_y}(t) e^{ik_x x/L} \sin(k_y y/d), \tag{3}$$

where $\widehat{\psi}_{k_x,k_y}$ is the amplitude of the (k_x, k_y) mode of ψ, and (N_x, N_y) denotes the number of aliased modes in the x and y directions. We decompose θ in the same way. A third-order Runge-Kutta scheme is used for time advancement and the aliasing errors are removed with the two-thirds dealiasing rule [44]. For $\mathrm{Ra} < 10^6$ a resolution of $N_x = N_y = 128$ is used, while for $\mathrm{Ra} \geqslant 10^6$, we fix the resolution to $N_x = N_y = 256$. All our runs were integrated to at least 10^4 eddy turnover times. Integrations for such very long times are necessary to accumulate reliable statistics for the zonal flow reversals. To verify our findings, some runs were repeated at a finer resolution.

We are interested in quantifying the transitions of the large scale flow as the Rayleigh number is increased. Thus, we consider the largest scale mode $\widehat{\psi}_{0,1}(t)$, defined as

$$\widehat{\psi}_{0,1}(t) = \frac{1}{\pi^2 L d} \int_0^{2\pi L} \int_0^{\pi d} \psi(x, y, t) \sin(y/d)\, dy\, dx. \tag{4}$$

The emergence of $\widehat{\psi}_{0,1}$ spontaneously breaks the centerline symmetry about $y = \pi d/2$ to form a zonal mean profile. The onset of the $\widehat{\psi}_{0,1}$ mode is currently being studied in detail and will be reported elsewhere.

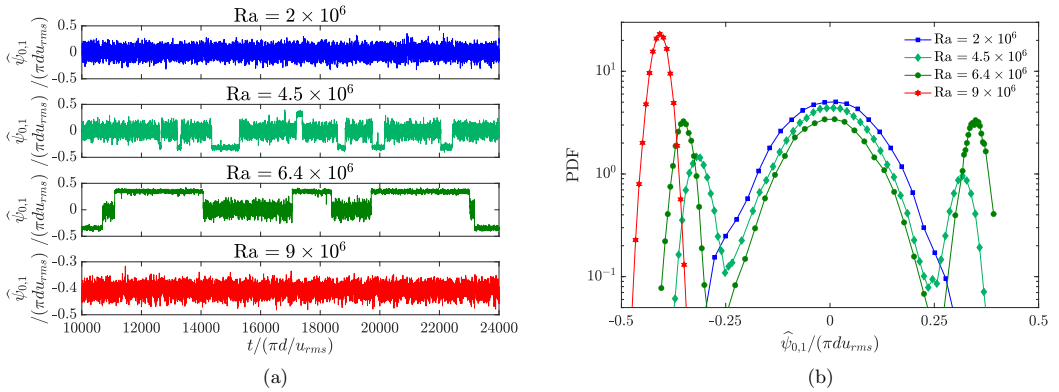

FIG. 1. (a) Time series of the normalized large scale mode $\widehat{\psi}_{0,1}$ for $\Gamma = 2$ and (b) their corresponding PDFs for different values of Ra.

III. RESULTS

We first focus on simulations of an anisotropic domain with $\Gamma = 2$. Time series of $\widehat{\psi}_{0,1}$ normalized appropriately (using the depth πd and the rms velocity $u_{\rm rms} = \langle |\nabla \psi|^2 \rangle_{\mathbf{x},t}^{1/2}$ where $\langle \cdot \rangle_{\mathbf{x},t}$ denotes a spatiotemporal average) and their corresponding probability density functions (PDFs) are displayed in Fig. 1 for different values of Ra.

At $\mathrm{Ra} = 2 \times 10^6$, the time series is turbulent with the amplitude of $\widehat{\psi}_{0,1}$ fluctuating randomly around the zero mean. This is an example of nonshearing convection as $\widehat{\psi}_{0,1}$ does not break the centerline symmetry in a statistical sense, i.e., $\langle \widehat{\psi}_{0,1} \rangle = 0$, where $\langle \cdot \rangle$ denotes a time average. The PDF of this time series (blue squares) is close to Gaussian. For nonshearing convection, the resulting flow is characterized by the usual convection rolls.

At $\mathrm{Ra} = 4.5 \times 10^6$, the PDF (green diamonds) has three distinct peaks. This follows the first bifurcation where the system transitions from an approximate Gaussian to a trimodal distribution with two symmetric maxima either side of the peak around $\widehat{\psi}_{0,1} = 0$. This behavior is related to the emergence of two symmetric shearing states, and the time series is characterized by abrupt and random transitions between these two states (i.e., $\langle \widehat{\psi}_{0,1} \rangle > 0$ and $\langle \widehat{\psi}_{0,1} \rangle < 0$) and the nonshearing state (i.e., $\langle \widehat{\psi}_{0,1} \rangle \approx 0$).

For $\mathrm{Ra} = 6.4 \times 10^6$ we get random reversals of the large scale flow with a PDF (green circles) which is again trimodal. The system now spends longer intervals in the symmetric shearing states, and the corresponding peaks in the PDF are therefore stronger compared with the peak at $\langle \widehat{\psi}_{0,1} \rangle \approx 0$. As we keep increasing Ra, the reversals become rarer until we get to a transition where no more large scale flow reversals are observed. This is seen in the case with $\mathrm{Ra} = 9 \times 10^6$ where the system was never observed to reverse, remaining stuck in one of the shearing states, and the corresponding PDF (red hexagons) is unimodal with a nonzero mean. The PDF for the largest $\mathrm{Ra} = 9 \times 10^6$ chooses either a positive or negative value of $\widehat{\psi}_{0,1}$ depending on the initial condition. This unimodal distribution indicates that ensemble averaging is not equivalent to time averaging for this system.

To understand the flow structure of the different states, in Fig. 2 we plot the zonal mean flow profile

$$U(y,t) = -\frac{1}{2\pi L} \int_0^{2\pi L} \psi_y(x,y,t)\, dx \tag{5}$$

normalized with u_{rms}, for the flow with $\mathrm{Ra} = 6.4 \times 10^6$. The light-colored curves indicate instantaneous realizations of the zonal mean flow profile at different times. These times correspond

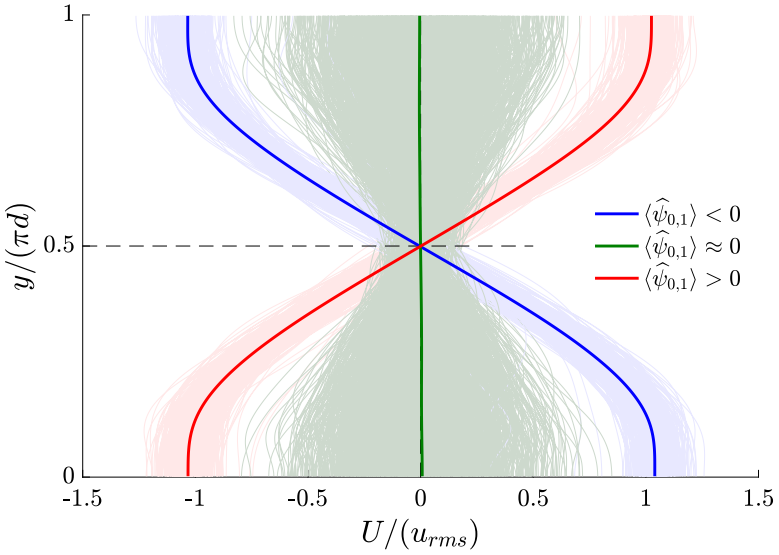

FIG. 2. Time averaged zonal mean flow profiles when $\langle\widehat{\psi}_{0,1}\rangle < 0$ (blue), $\langle\widehat{\psi}_{0,1}\rangle \approx 0$ (green), and $\langle\widehat{\psi}_{0,1}\rangle > 0$ (red) for $\mathrm{Ra} = 6.4 \times 10^6$ and $\Gamma = 2$. The light-colored curves represent instantaneous zonal mean flow profiles and the thicker curves are the averages of these.

to $\langle\widehat{\psi}_{0,1}\rangle < 0$ for the light blue curves, to $\langle\widehat{\psi}_{0,1}\rangle > 0$ for the light red curves, and to $\langle\widehat{\psi}_{0,1}\rangle \approx 0$ for the light green curves. The thicker blue, red, and green curves are the time averages of the corresponding light-colored curves. The shear developed in the two shearing states is antisymmetric with respect to the centerline $y/(\pi d) = 1/2$. When $\langle\widehat{\psi}_{0,1}\rangle > 0$, we observe strong eastward and westward moving flow in the upper half ($1/2 < y/\pi d < 1$) and lower half ($0 < y/\pi d < 1/2$) of the domain, respectively. The opposite is true when $\langle\widehat{\psi}_{0,1}\rangle < 0$, while there is no time-averaged zonal mean flow when $\langle\widehat{\psi}_{0,1}\rangle \approx 0$ even though some instantaneous profiles can be considered having fairly strong shear due to the fluctuations of $\widehat{\psi}_{0,1}$ around zero. The transition between the two shearing states denotes the reversals of the large scale zonal flow, which occur on a time scale much longer than the eddy turnover time.

To quantify the instantaneous heat transport, we consider the time-dependent Nusselt number,

$$\mathrm{Nu}(t) = 1 + \frac{\pi d}{\kappa \Delta T}\langle\theta\psi_x\rangle_{\mathbf{x}}, \tag{6}$$

where $\langle\cdot\rangle_{\mathbf{x}}$ denotes a spatial average. Within the regime of zonal flow reversals, we observe significant reduction in the heat transport while the system is in a shearing state. Figure 3 shows instantaneous realizations of the temperature field $T = \Delta T(1 - y/\pi d) + \theta$ along with the time series of the normalized $\widehat{\psi}_{0,1}$ and Nu at $\mathrm{Ra} = 6.4 \times 10^6$. In shearing states such as in Figs. 3(a) and 3(c), the shear prevents thermal plumes from traversing the domain, decreasing the convective heat transport. In nonshearing states such as in Fig. 3(b), the shear is not strong enough to suppress thermal plumes, and convection rolls are sustained, promoting convective heat transport. This observation is supported further by the time average values that the Nusselt number takes in Fig. 3 depending on when the system is in a shearing or nonshearing state, with $\langle\mathrm{Nu}\rangle = 24.3$ or 34, respectively.

Now, we explore the effect of the aspect ratio on the transitions of the large scale mode by considering an isotropic domain with $\Gamma = 1$. At $\mathrm{Ra} = 6 \times 10^5$ the time series of $\widehat{\psi}_{0,1}/(\pi d u_{rms})$ is characterized by abrupt and random transitions between two symmetric shearing states [see Fig. 4(a)].

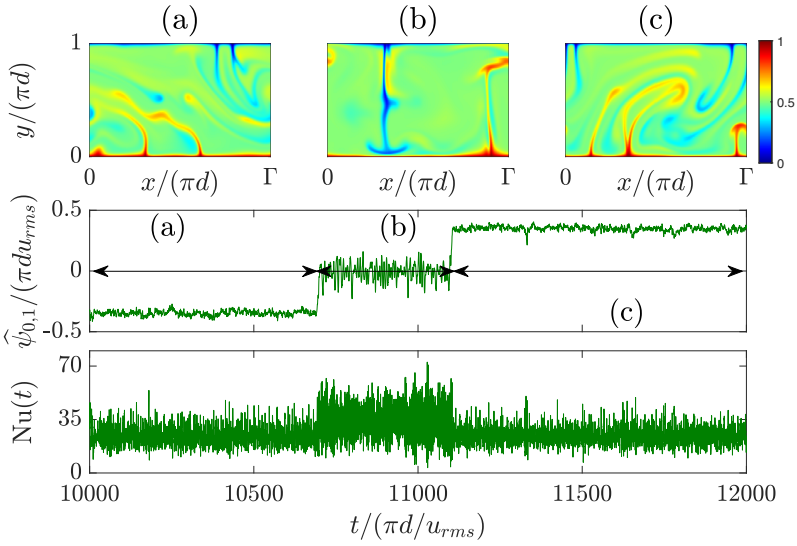

FIG. 3. The top row of figures shows instantaneous realizations of the temperature field $T = \Delta T(1 - y/\pi d) + \theta$ for Ra $= 6.4 \times 10^6$ and $\Gamma = 2$. The middle and bottom rows have associated time series for $\widehat{\psi}_{0,1}$ and Nu(t) respectively, with times (a), (b), and (c) annotated.

In contrast with the case where $\Gamma = 2$, we no longer observe a transition to a nonshearing state within the regime that zonal flow reversals occur. In addition, the bifurcation diagrams of $\langle\widehat{\psi}_{0,1}\rangle$ for $\Gamma = 2$ [Fig. 4(b)] and $\Gamma = 1$ [Fig. 4(c)] demonstrate that the nature of bifurcations with respect to the Rayleigh number depends on the aspect ratio. For $\Gamma = 2$, we observe two bifurcations in

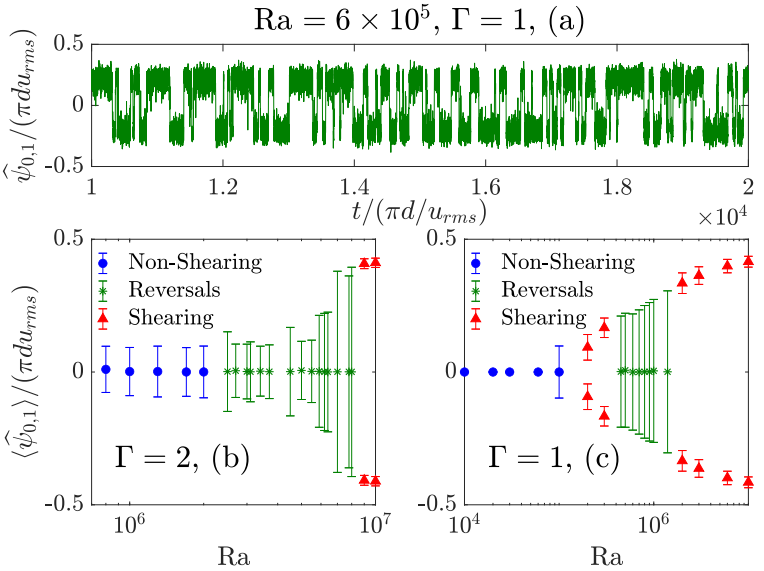

FIG. 4. (a) Time series of $\widehat{\psi}_{0,1}$ for Ra $= 6 \times 10^5$ and $\Gamma = 1$. Bifurcation diagrams for (b) $\Gamma = 2$ and (c) $\Gamma = 1$. Error bars show one standard deviation in the time series of $\widehat{\psi}_{0,1}$. The nonshearing, shearing, and reversing regimes are highlighted by (●), (▲) and (∗), respectively.

the system as Ra increases. As we have already seen, the first bifurcation designates the onset of random zonal flow reversals between two symmetric shearing states and a nonshearing state, and is characterized by the transition from a Gaussian to a trimodal distribution for the time series of $\widehat{\psi}_{0,1}$ [see Fig. 1(b)]. The second bifurcation is characterized by the transition of a trimodal to a one-sided unimodal distribution, which designates the disappearance of zonal flow reversals in the system. On the other hand, for $\Gamma = 1$ we observe three bifurcations [see Fig. 4(c)]. In this case, the first bifurcation occurs from a nonshearing state to a persistent shearing state, and this is characterized by a transition from a Gaussian to a one-sided unimodal distribution of $\widehat{\psi}_{0,1}$. The second bifurcation for $\Gamma = 1$ is the one that designates the onset of random zonal flow reversals. However, note here that the transition is from a one-sided unimodal distribution to a bimodal distribution of $\widehat{\psi}_{0,1}$ as it can be inferred from Figs. 4(a) and 4(c). Finally, the third bifurcation for $\Gamma = 1$ is the one that designates the disappearance of zonal flow reversals with a transition from a bimodal to a one-sided unimodal distribution. Note that when $\Gamma = 1$ the regime of zonal flow reversals occurs at values of Ra which are an order of magnitude smaller than when $\Gamma = 2$. Moreover, as the aspect ratio decreases, shearing states emerge at lower Rayleigh numbers [see Fig. 4(c)], in agreement with recent results [15].

IV. CONCLUSIONS

In summary, for a moderate Prandtl number fluid in 2D Rayleigh-Bénard convection, we observe the emergence of a large scale zonal flow, whose dynamics are dominated by the largest scale mode $\widehat{\psi}_{0,1}$. As the Rayleigh number increases, we find large scale flow transitions between long-lived metastable states within the turbulent regime of the system. These transitions are seen in the PDF of the time series of the $\widehat{\psi}_{0,1}$ mode. For aspect ratio $\Gamma = 2$, the PDF transitions first from a Gaussian to a trimodal distribution, signifying the onset of reversals between two symmetric shearing states and a nonshearing state. The zonal flow reversals suppress the convective heat transfer as thermal plumes are not able to traverse the layer. Then, as Ra increases further, a second transition occurs from a trimodal to a one-sided unimodal distribution, where reversals cease to exist for the whole duration of the simulation. For $\Gamma = 1$, similar flow transitions are observed but the reversals in this case occur between two symmetric shearing states giving a bimodal PDF for the large scale mode. A similar set of bifurcations on a turbulent background leading to the emergence and disappearance of reversals in the large scale zonal mean flow has been observed in other contexts [28,45–47], and hence we believe that they are generic.

In this article, we have focused on the parameter range in which the dynamics of zonal flow reversals are observed. The physical mechanism behind the reversals of the large scale zonal flow remains an open question. The truncated Euler equations could be one way to theoretically understand these dynamics further like in [28,45]. Nevertheless, it should be noted that the mechanism for zonal flow reversals must differ markedly from the one that has been used to explain reversals of the LSC in Rayleigh-Bénard convection in a box geometry with no-slip walls, where the boundary layers [34] and vortex reconnection [37] play a crucial role for reversals. With free-slip walls, it has been suggested that the nonlinearity in the temperature equation plays a vital role on the reversals of the LSC [39]. However, buoyancy only does work on the vertical flow, meaning that the dynamics of the $\widehat{\psi}_{0,1}$ mode partially decouples from the temperature equation since $\partial_x(\widehat{\theta}_{0,1}(t)\sin(y/d)) = 0$. This issue, and a wider parameter space, is explored in an ongoing study, which we aim to report in detail in the near future.

ACKNOWLEDGMENTS

We would like to thank K. Seshasayanan for his comments on an initial version of this manuscript. The computations were performed using the departmental computing facilities of the Mathematical Institute and ARC, the High Performance Computing system of the University of Oxford.

[1] M. Heimpel, J. Aurnou, and J. Wicht, Simulation of equatorial and high-latitude jets on Jupiter in a deep convection model, Nature **438**, 193 (2005).
[2] D. Kong, K. Zhang, and G. Schubert, Origin of Jupiter's cloud-level zonal winds remains a puzzle even after Juno, Proc. Natl. Acad. Sci. USA **115**, 8499 (2018).
[3] Y. Kaspi *et al.*, Jupiter's atmospheric jet streams extend thousands of kilometres deep, Nature **555**, 223 (2018).
[4] N. A. Maximenko, B. Bang, and H. Sasaki, Observational evidence of alternating zonal jets in the world ocean, Geophys. Res. Lett. **32**, L12607 (2005).
[5] K. Richards, N. Maximenko, F. Bryan, and H. Sasaki, Zonal jets in the pacific ocean, Geophys. Res. Lett. **33**, L03605 (2006).
[6] B. T. Nadiga, On zonal jets in oceans, Geophys. Res. Lett. **33**, L10601 (2006).
[7] P. H. Diamond, S.-I. Itoh, K. Itoh, and T. S. Hahm, Zonal flows in plasma—a review, Plasma Phys. Controlled Fusion **47**, R35 (2005).
[8] A. Fujisawa, A review of zonal flow experiments, Nucl. Fusion **49**, 013001 (2008).
[9] X. Zhang, D. P. M. van Gils, S. Horn, M. Wedi, L. Zwirner, G. Ahlers, R. E. Ecke, S. Weiss, E. Bodenschatz, and O. Shishkina, Boundary Zonal Flow in Rotating Turbulent Rayleigh-Bénard Convection, Phys. Rev. Lett. **124**, 084505 (2020).
[10] P. L. Read, T. N. L. Jacoby, P. H. T. Rogberg, R. D. Wordsworth, Y. H. Yamazaki, K. Miki-Yamazaki, R. M. B. Young, J. Sommeria, H. Didelle, and S. Viboud, An experimental study of multiple zonal jet formation in rotating, thermally driven convective flows on a topographic beta-plane, Phys. Fluids **27**, 085111 (2015).
[11] R. Krishnamurti and L. N. Howard, Large-scale flow generation in turbulent convection, Proc. Natl. Acad. Sci. USA **78**, 1981 (1981).
[12] D. Goluskin, H. Johnston, G. R. Flierl, and E. A. Spiegel, Convectively driven shear and decreased heat flux, J. Fluid Mech. **759**, 360 (2014).
[13] E. P. van der Poel, R. Ostilla-Mónico, R. Verzicco, and D. Lohse, Effect of velocity boundary conditions on the heat transfer and flow topology in two-dimensional Rayleigh-Bénard convection, Phys. Rev. E **90**, 013017 (2014).
[14] J. von Hardenberg, D. Goluskin, A. Provenzale, and E. A. Spiegel, Generation of Large-Scale Winds in Horizontally Anisotropic Convection, Phys. Rev. Lett. **115**, 134501 (2015).
[15] Q. Wang, K. L. Chong, R. J. A. M. Stevens, R. Verzicco, and F. Lohse, From zonal flow to convection rolls in Rayleigh-Bénard convection with free-slip plates, J. Fluid Mech. **905**, A21 (2020).
[16] M. J. Schmeits and H. A. Dijkstra, Bimodal behavior of the Kuroshio and the Gulf Stream, J. Phys. Oceanogr. **31**, 3435 (2001).
[17] P. S. Marcus, Prediction of a global climate change on Jupiter, Nature **428**, 828 (2004).
[18] I. Wygnanski, F. Champagne, and B. Marasli, On the large-scale structures in two-dimensional, small-deficit, turbulent wakes, J. Fluid Mech. **168**, 31 (1986).
[19] O. Cadot, A. Evrard, and L. Pastur, Imperfect supercritical bifurcation in a three-dimensional turbulent wake, Phys. Rev. E **91**, 063005 (2015).
[20] R. Labbé, J. Pinton, and S. Fauve, Study of the von Kármán flow between coaxial corotating disks, Phys. Fluids **8**, 914 (1996).
[21] F. Ravelet, L. Marié, A. Chiffaudel, and F. Daviaud, Multistability and Memory Effect in a Highly Turbulent Flow: Experimental Evidence for a Global Bifurcation, Phys. Rev. Lett. **93**, 164501 (2004).
[22] A. de la Torre and J. Burguete, Slow Dynamics in a Turbulent von Kármán Swirling Flow, Phys. Rev. Lett. **99**, 054101 (2007).
[23] M. Berhanu, R. Monchaux, S. Fauve, N. Mordant, F. Pétrélis, A. Chiffaudel, F. Daviaud, B. Dubrulle, L. Marié, F. Ravelet *et al.*, Magnetic field reversals in an experimental turbulent dynamo, Europhys. Lett. **77**, 59001 (2007).
[24] R. J. A. M. Stevens, J.-Q. Zhong, H. J. H. Clercx, G. Ahlers, and D. Lohse, Transitions between Turbulent States in Rotating Rayleigh-Bénard Convection, Phys. Rev. Lett. **103**, 024503 (2009).

[25] P. Wei, S. Weiss, and G. Ahlers, Multiple Transitions in Rotating Turbulent Rayleigh-Bénard Convection, Phys. Rev. Lett. **114**, 114506 (2015).
[26] S. G. Huisman, R. C. Van Der Veen, C. Sun, and D. Lohse, Multiple states in highly turbulent Taylor–Couette flow, Nat. Commun. **5**, 3820 (2014).
[27] G. Michel, J. Herault, F. Pétrélis, and S. Fauve, Bifurcations of a large-scale circulation in a quasi-bidimensional turbulent flow, Europhys. Lett. **115**, 64004 (2016).
[28] V. Dallas, K. Seshasayanan, and S. Fauve, Transitions between turbulent states in a two-dimensional shear flow, Phys. Rev. Fluids **5**, 084610 (2020).
[29] U. Frisch, *Turbulence: The Legacy of AN Kolmogorov* (Cambridge University Press, Cambridge, U.K., 1995).
[30] K. R. Sreenivasan, A. Bershadskii, and J. J. Niemela, Mean wind and its reversal in thermal convection, Phys. Rev. E **65**, 056306 (2002).
[31] R. Ni, S.-D. Huang, and K.-Q. Xia, Reversals of the large-scale circulation in quasi-2D Rayleigh-Bénard convection, J. Fluid Mech. **778**, R5 (2015).
[32] Y.-C. Xie, G.-Y. Ding, and K.-Q. Xia, Flow Topology Transition via Global Bifurcation in Thermally Driven Turbulence, Phys. Rev. Lett. **120**, 214501 (2018).
[33] M. Breuer and U. Hansen, Turbulent convection in the zero Reynolds number limit, Europhys. Lett. **86**, 24004 (2009).
[34] K. Sugiyama, R. Ni, R. J. A. M. Stevens, T. S. Chan, S.-Q. Zhou, H.-D. Xi, C. Sun, S. Grossmann, K.-Q. Xia, and D. Lohse, Flow Reversals in Thermally Driven Turbulence, Phys. Rev. Lett. **105**, 034503 (2010).
[35] T. Yanagisawa, Y. Yamagishi, Y. Hamano, Y. Tasaka, and Y. Takeda, Spontaneous flow reversals in Rayleigh-Bénard convection of a liquid metal, Phys. Rev. E **83**, 036307 (2011).
[36] K. Petschel, M. Wilczek, M. Breuer, R. Friedrich, and U. Hansen, Statistical analysis of global wind dynamics in vigorous Rayleigh-Bénard convection, Phys. Rev. E **84**, 026309 (2011).
[37] M. Chandra and M. K. Verma, Flow Reversals in Turbulent Convection via Vortex Reconnections, Phys. Rev. Lett. **110**, 114503 (2013).
[38] B. Podvin and A. Sergent, A large-scale investigation of wind reversal in a square Rayleigh-Bénard cell, J. Fluid Mech. **766**, 172 (2015).
[39] M. K. Verma, S. C. Ambhire, and A. Pandey, Flow reversals in turbulent convection with free-slip walls, Phys. Fluids **27**, 047102 (2015).
[40] H.-D. X. Ao Xu, and Xin Chen, Tristable flow states and reversal of the large-scale circulation in two-dimensional circular convection cells, J. Fluid Mech. **910**, A33 (2021).
[41] L. P. Kadanoff, *Statistical Physics: Statics, Dynamics and Renormalization* (World Scientific, Singapore, 2000).
[42] S. A. Orszag and D. Gottlieb, *Numerical Analysis of Spectral Methods: Theory and Application* (Society for Industrial and Applied Mathematics, Philadelphia, 1977).
[43] K. Seshasayanan, V. Dallas, and S. Fauve, Bifurcations of a plane parallel flow with Kolmogorov forcing, arXiv:2004.12418.
[44] D. O. Gómez, P. D. Mininni, and P. Dmitruk, Parallel simulations in turbulent MHD, Phys. Scr. T **116**, 123 (2005).
[45] V. Shukla, S. Fauve, and M.-E. Brachet, Statistical theory of reversals in two-dimensional confined turbulent flows, Phys. Rev. E **94**, 061101(R) (2016).
[46] S. Fauve, J. Herault, G. Michel, and F. Pétrélis, Instabilities on a turbulent background, J. Stat. Mech. (2017) 064001.
[47] M. Pereira, C. Gissinger, and S. Fauve, $1/f$ noise and long-term memory of coherent structures in a turbulent shear flow, Phys. Rev. E **99**, 023106 (2019).